electronics

MDPI

Article

Performance Validation of High-Speed Motor for Electric Turbochargers Using Various Test Methods

Tae-Woo Lee [1] and Do-Kwan Hong [1,2,*]

[1] Electric Machines and Drives Research Center, Korea Electrotechnology Research Institute, Changwon 51543, Republic of Korea; twlee@keri.re.kr
[2] Department of Electric Energy Conversion Engineering, University of Science and Technology, Changwon 51543, Republic of Korea
* Correspondence: dkhong@keri.re.kr; Tel.: +82-(0)10-9601-9234

Abstract: As environmental regulations on automotive exhaust gas are gradually strengthened to cope with climate change, internal combustion engines, including those in hybrid electric vehicles, are continuously being downsized. Supercharging technologies are essential to compensate for the reduced engine power. One of the supercharging technologies, the turbocharger, has a response delay in the low-speed region, which is known as turbo lag. Various technologies have emerged to reduce turbo lag. Recently, electric supercharging technologies capable of reducing turbo lag using high-speed motors have been developed and commercialized. However, they are difficult to obtain for high-speed motors because of the cost of load performance test equipment. For this reason, many previous studies have compared analysis and experiment results under no-load conditions, or they have estimated performance in the high-speed region from results at low speed with light loads. This makes it difficult to know exactly how the performance of the motor is affected under loads applied to an actual system. In this study, performance test evaluation was conducted using a high-speed torque sensor, eddy current brake, and inertial dynamometer. Input/output power and efficiency were calculated using the measured voltage, current and output side torque and speed, and the results were compared.

Keywords: electric turbocharger; high-speed motor; performance test; surface mounted permanent magnet synchronous motor

Citation: Lee, T.-W.; Hong, D.-K. Performance Validation of High-Speed Motor for Electric Turbochargers Using Various Test Methods. *Electronics* **2023**, *12*, 2937. https://doi.org/10.3390/electronics12132937

Academic Editor: Adel M. Sharaf

Received: 28 April 2023
Revised: 29 June 2023
Accepted: 3 July 2023
Published: 4 July 2023

1. Introduction

Internal combustion engines (ICEs), including those in hybrid electric vehicles (HEVs), are being downsized as environmental rules on vehicle exhaust gas become increasingly stringent, to combat climate change. Engine downsizing involves approaches which shrink the engine's displacement to cut down on fuel use and carbon dioxide (CO_2) emissions. Using what are referred to as forced induction systems (FISs) [1,2], a significant amount of fresh air is blasted into the engine to make up for insufficient performance. One of the supercharging methods, the turbocharger, has a turbo lag, or delayed response, in the low-speed range. Several methods have been created to reduce turbo lag, but recently, electric supercharging technologies that use high-speed motors have been developed and are commercially available. However, one limitation of the electric turbocharger is that it requires a lot of power to operate, and there has been a recent trend toward applying it to mild hybrid vehicles with 48 V_{dc} battery systems rather than 12 V_{dc} battery systems. Figure 1 and Table 1 [1–21] present the literature and research on electric turbochargers for automobiles with battery systems ranging from 12 to 48 V_{dc} for the previous 20 years.

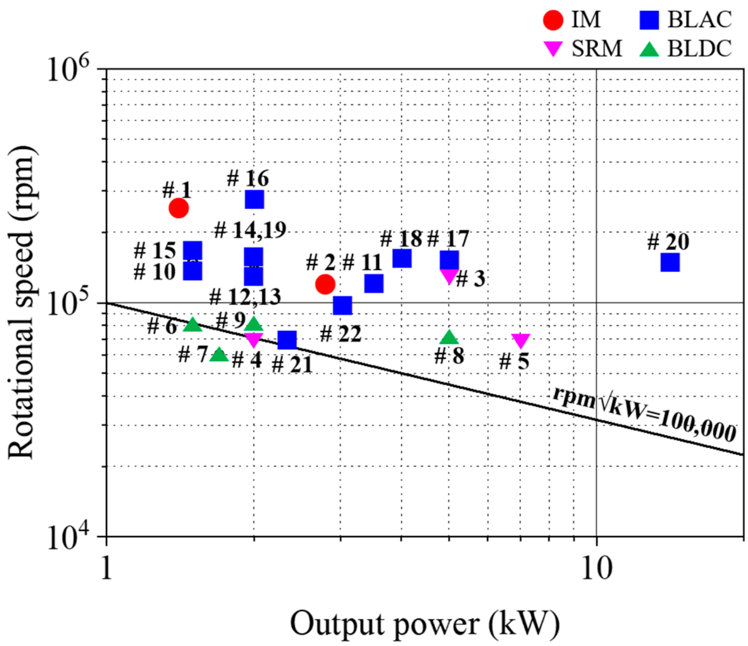

Figure 1. High-speed motors of electric turbocharger output power versus speed for different machine topologies.

Table 1. High-speed machines for electric turbochargers with 12 V_{dc} to 48 V_{dc} battery systems.

No.	Motor	Power (kW)	Speed (krpm)	Voltage (V_{dc})	Topology	Designed/Studied by
1	IM	1.4	250	12	EAT	Honeywell
2		2.8	120	48	EAT	Honeywell
3 [1]	SRM	5.0	140	12/24	EAT	Loughborough Univ.
4		2.0	70	12	TEDC	Valeo/CPT
5 [2]		7.0	70	48	TEDC	Valeo/CPT
6	BLDC	1.5	80	24	TEDC	WEM-PEC
7		1.7	60	12	TEDC	BorgWarner
8 [3]		5.0	70	48	TEDC	BorgWarner
9		2.0	80	48	TEDC	MMT
10	BLAC	1.5	150	12	EC	Nagaoka Univ.
11		3.5	120	48	EC	Technische Univ.
12		2.0	140	12	EC	MHI
13		2.0	140	12	EAT	MHI
14		2.0	150	12	EAT	IHI
15		1.5	160	12	EAT	G + L innotec
16		2.0	280	12	EAT	EcoMotor
17		5.0	150	48	EAT	EcoMotor
18		4.0	150	48	EAT	Hanyang Univ.
19		2.0	150	12	EAT	Aeristech
20		14.0	150	48	EAT	Aeristech
21		2.3	70	48	TEDC	KERI/Keyyang
22		3.0	100	48	TEDC	KERI/Keyyang

[1] Applied to Caterpillar 7.01-L heavy duty vehicles diesel engine. [2] Applied to Audi SQ7 4.0-L TDI engine. [3] Applied to Mercedes-Benz 3.0-L M256 engine.

As shown in Figure 1, high-speed motors often operate at speeds above 10,000 rpm and 100,000 rpm$\sqrt{}$kW or more. Table 1 shows three types of high-speed motors used in electric turbochargers, Induction motors (IM), switching reluctance motors (SRM), and permanent magnet synchronous motors (PMSM). The IMs are appropriate as an electric motor for electric turbochargers and are structurally sturdy even under the strong centrifugal force produced by high-speed rotation, but their efficiency is rather low due to additional loss from the induced current generated by the rotor. Because the rotors do not have PMs, SRMs are also ideal for electric turbochargers that are utilized for high-speed operation and at high ambient temperature. However, because of their doubly prominent structure and quick change in magneto-motive force when the switch is on or off, they have the drawbacks of torque ripple, noise, and vibration. PMSMs are distinguished by their high power density and efficiency due to their utilization of rare earth magnets and great energy integration. To prevent demagnetization in high-temperature applications, such as electric turbochargers, PMs with a high working temperature must be utilized [2].

In synchronous motors, the switching frequency typically increases along with the number of poles. In high-speed synchronous motors, the number of poles is therefore chosen with the switching frequency in mind. For the two poles with the fewest poles, surface-mounted permanent magnets (SPMs) are more frequently employed than interior permanent magnets (IPMs). To stop the PMs from being dispersed, a sleeve or a container should be employed when an SPM-type rotor is used in a high-speed motor.

Lee et al. accurately described the topology of the following electric forced induction systems (EFISs) according to where the electric motor is located: electric compressor (EC), electrically assisted turbocharger (EAT), electrically split turbocharger (EST), and turbocharger with an additional electrically driven compressor (TEDC) [1,2]. TEDC and EAT are the two primary variables in Table 1. The demagnetization and cooling of the PMs by the hot exhaust should be taken into account if a PMSM is utilized for the EAT topology since the motor is positioned between the compressor wheel and the turbine. Due to an increase in rotor inertia caused by the addition of an electric motor to the turbocharger shaft, the response performance should also be verified.

The Korea Electrotechnology Research Institute (KERI) (Changwon, Republic of Korea) and Keyyang Precision Co., Ltd. (Gimcheon-si, Republic of Korea) which is a manufacturer of conventional turbochargers in South Korea, developed the electric turbocharger system. As shown in Figure 2, it is designed to fit 1.6 L diesel automobiles and has a power output of 3 kW at 100,000 rpm. It reduces turbo lag to within 0.4 s. For high-power density and efficiency, we chose a high-speed surface-mounted permanent magnet synchronous motor (SPMSM). The TEDC topology was chosen to provide thermal stability by separating the electric motor from the traditional turbocharger. This also has the benefit of increasing transient response performance [2,21–23].

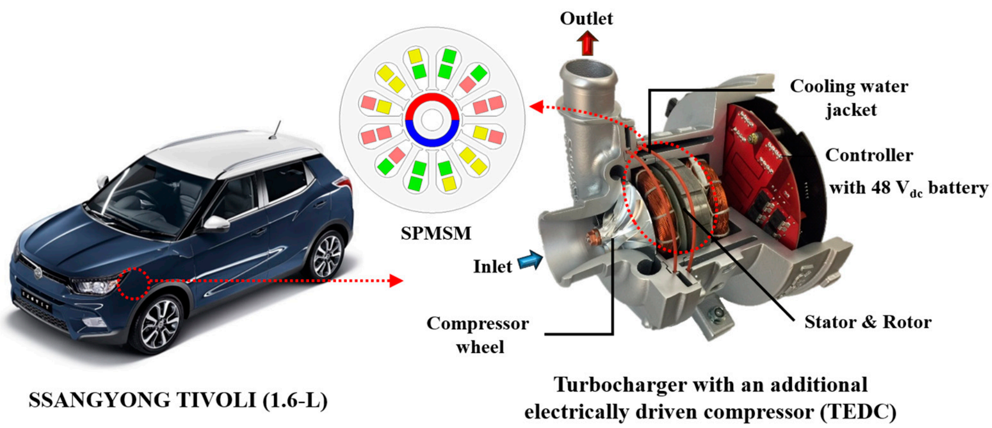

Figure 2. KERI and Keyyang Precision's turbocharger with an additional electrically driven compressor (TEDC).

Because of the high cost, it is challenging to build load test equipment for high-speed motors. Instead, in many study scenarios, the observed loss values under no-load conditions are compared to load tests and analysis values, or the performance of high-speed regions is approximated based on performance at low speeds with modest loads [10,11,24–29]. It is also challenging to precisely determine how the motor performs when a load is applied to an actual system. In this study, performance tests were carried out by employing an inertial dynamometer, an eddy current brake, and a high-speed torque sensor. The observed voltage, current, torque, and speed were used to determine the input/output power and efficiency, and the results were compared.

2. High-Speed Motor for Electric Turbocharger

In previous studies [2,20–23], we proposed rotor and stator models using various poles/slots combinations and winding methods, and we designed a 3 kW, 100,000 rpm SPMSM through mechanical analysis as well as electromagnetic finite element analysis (FEA). The FEA results of the designed motor at a rated speed are shown in Figure 3 and Table 2. The copper loss was calculated by multiplying the square of the current flowing in each phase by the winding resistance. The core loss of the rotor and stator was calculated using the Steinmetz equation with the flux density and frequency of the rated speed. The eddy current loss in the PMs was calculated by the finite element method using the Maxwell equations and the magnetic vector potential. Mechanical loss is usually 2–3% of the total output, and it was assumed to be 2.5% of the total output. Then, the prototype was fabricated and the performance of the motor was evaluated using a motor/generator (M/G) dynamometer with a reaction torque sensor and a variable resistor, as illustrated in Figure 4. In a typical M/G dynamometer, the torque sensor is located between the motor and the generator, and since the allowable speed of the torque sensor must be greater than the operating speed of the test motor, the cost of a torque sensor for a high-speed motor is inevitably high. However, the reaction torque sensor used in Figure 4 is fixed between the housing and the jig of the test motor and calculates the torque using the shear stress generated when the torque is applied to the torque sensor, so it has the advantage of measuring the torque regardless of the operating speed of the test motor. The performance of the designed motor was verified by comparing it with FEA using the dynamometer in Figure 4, and as shown in Figure 5, the results confirmed that the transient response performance of 1.6 L diesel engine was improved by sufficiently reducing the turbo lag, which is a disadvantage of conventional turbochargers, even at 70,000 rpm [20]. The specifications for 1.6 L diesel engine is in Appendix A.

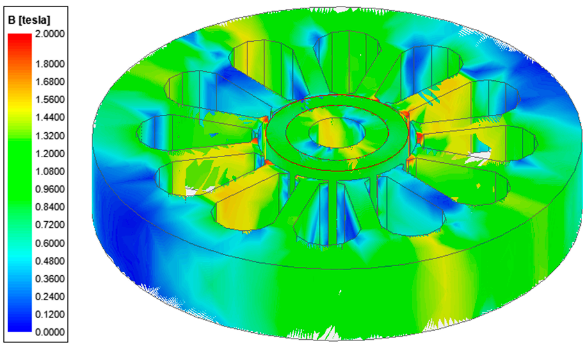

Figure 3. Flux density distribution of the motor designed for an electric turbocharger at rated speed.

Table 2. Results of 3D electromagnetic FEA and experiment for the designed motor at rated speed.

Parameter	Specification	FEA	Experiment
Torque (Nm)	0.2865	0.2865	0.2946
Power (kW)	3	3	3.084
Speed (rpm)	100,000	100,000	100,030
Efficiency (%)	≥93	94.0	94.10
Torque ripple (%)	-	1.32	-
Rotor core loss (W)	-	4.09	-
Stator core loss (W)	-	51.7	-
PM loss (W)	-	6.07	-
Winding loss (W)	-	55.7	-
Mechanical loss (W)	-	75.0	-

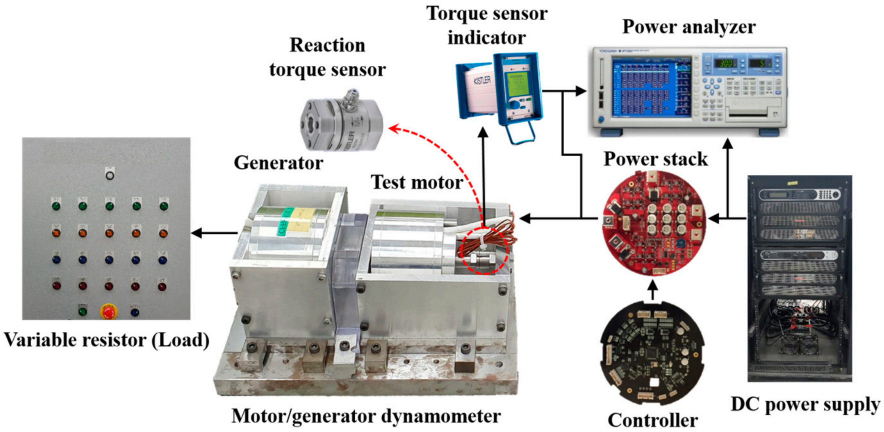

Figure 4. Configuration of motor/generator dynamometer with reaction torque sensor.

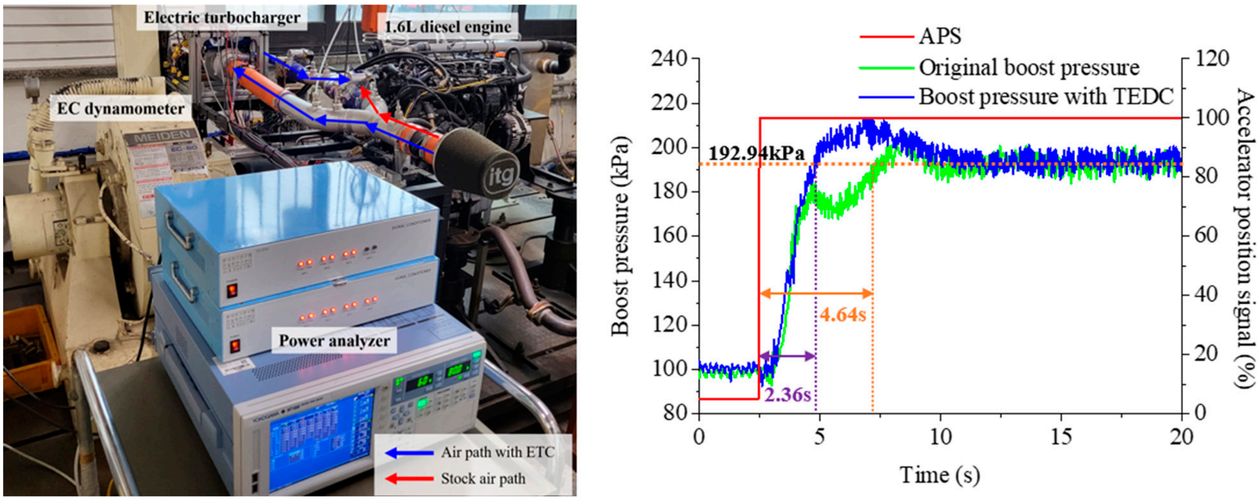

Figure 5. Configuration of engine dynamometer with electric turbocharger, 1.6 L diesel engine and experiment result.

Three performance tests were conducted under load conditions based on the results performed in Figure 4 at 70,000 rpm, as shown in Figure 6, and the procedure and method for each test are briefly introduced in the next section.

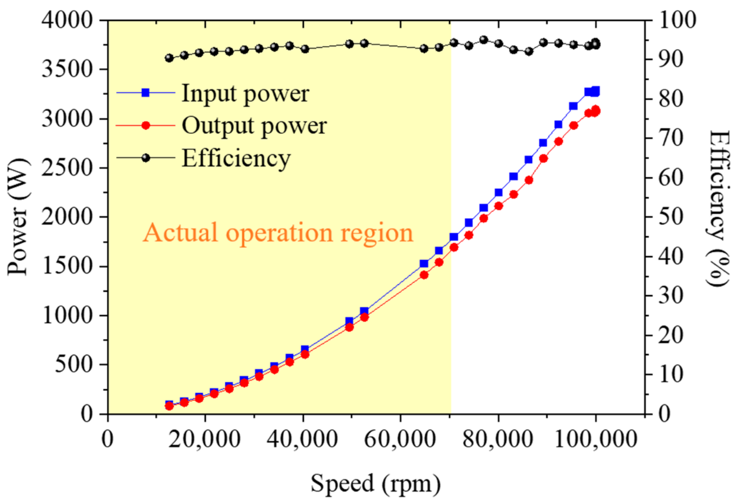

Figure 6. Experiment result of M/G dynamometer with reaction torque sensor.

3. Validation of Performance for High-Speed Motor via Various Experiments

The methods for the electric motors experiment were conducted according to IEC 60034-2-1, which is an international standard that specifies the methods for evaluating the efficiency and measuring the losses of rotating electrical machines, including both DC and AC synchronous and induction machines. This standard specifies methods for obtaining each loss of the motor from the test and for calculating the efficiency from these losses. For PMSMs, method 2-1-2A, a direct measurement of input and output, should be used, and the torque can be measured using an inline torque meter between the motor and the load or by means of a dynamometer with a cradle base construction [30]. Based on this information, a M/G dynamometer was constructed using a high-speed torque sensor, which is an inline torque meter type and a dynamometer with a cradle base structure using an eddy current brake. Another international standard, IEEE Standard 115™, specifies a torque measurement method using acceleration [31], and an inertial dynamometer was constructed based on this standard. The procedures for each experimental method are shown in Figure 7. Before constructing the dynamometer, the stability of the dynamometer system was analyzed, and each dynamometer was constructed according to the experimental method.

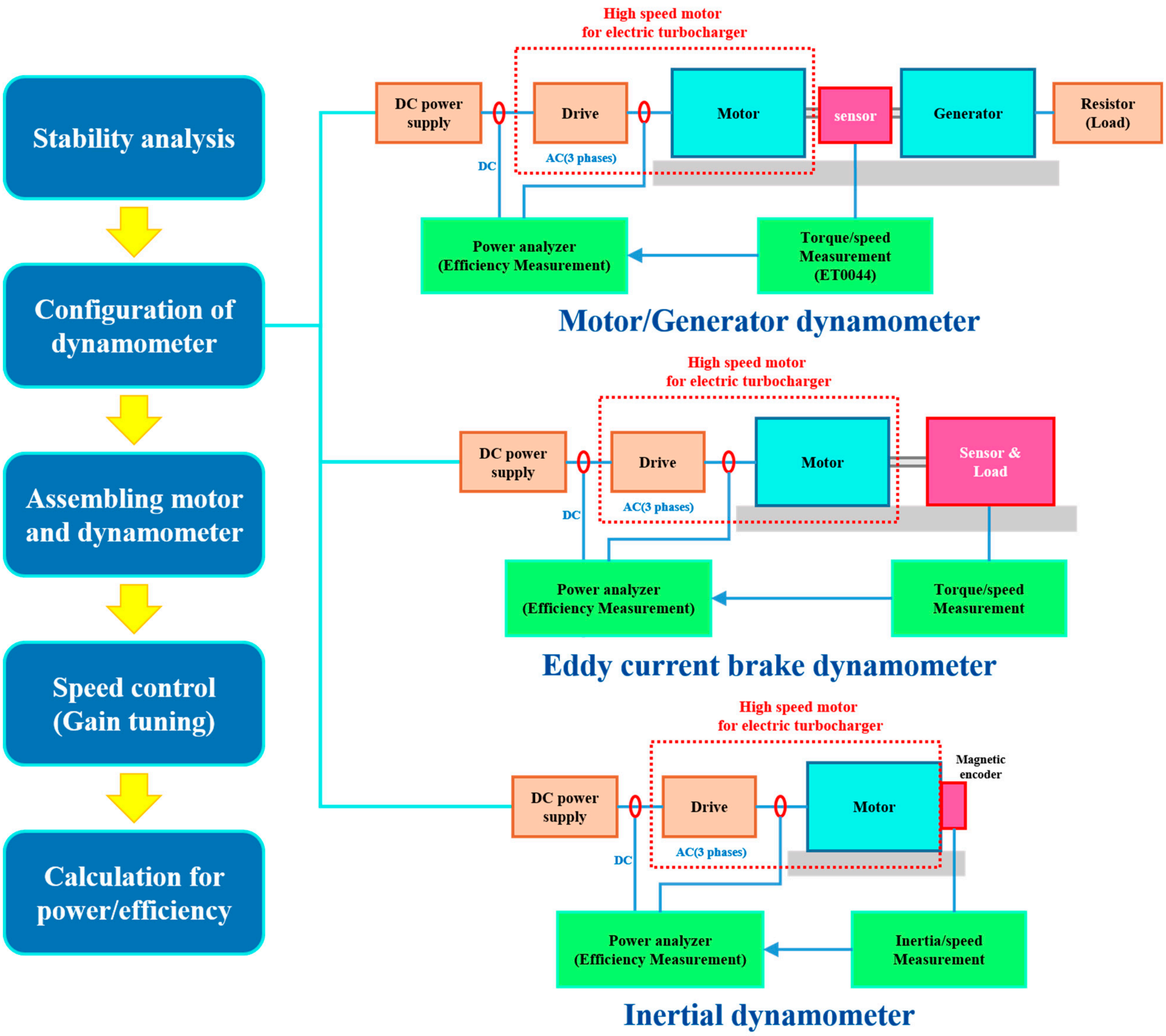

Figure 7. Procedure of motor experiment of motor and configuration of various dynamometers.

3.1. M/G Dynamometer with High-Speed Torque Sensor

Inline-type torque sensors, which are commonly used, can be classified into contact and non-contact types. They detect the torque applied to a rotating shaft using a strain gauge, and the contact-type torque sensor transmits the torque data acquired by the strain gauge through a slip ring and brush. However, this method is difficult to apply to high-speed rotating equipment. On the other hand, the non-contact type torque sensor transmits the torque data acquired by the strain gauge without contact, using radio frequency (RF) wireless, infrared communication, magnetic induction, etc. Therefore, it is used for high-speed rotating equipment. However, the price of non-contact type torque sensors increases as the rotation speed increases, and it is not easy to find a specification that allows a rotation speed of over 50,000 rpm. The high-speed torque sensor (ET004) used in this paper is the phase shift torque sensor from Torquemeters Ltd., which has a maximum allowable rotation speed of 120,000 rpm. It measures torque using gears and two coils located at each end of the torque sensor shaft. A coil encircles a gear at each end of the shaft. In the eddy current magnetic field of the coil, the gear generates a sine wave. When there is no load, the waves are parallel. The waves become out of phase with one another as a load is applied to the shaft. A phasemeter is then used to determine the phase displacement of these signals. A change of phase displacement of 100% always corresponds to the torque that twists the drive shaft through one tooth pitch [32]. Before constructing the dynamometer, 3D modeling was performed to build the dynamometer, and a stability analysis was performed to evaluate the structural stability of the operating area. Two major stability analyses were carried out: a modal analysis for the test motor and jig, and a dynamic characteristic analysis for the entire rotating system to determine if there were resonance points in the operating area. Figure 8 shows the modal analysis results for the test motor and jig, where the 1st natural frequency of the motor and jig was 1826.4 Hz. From the perspective of machine frequency, the maximum operating speed of 70,000 rpm corresponds to a machine frequency of approximately 1166.67 Hz, which indicates that the 1st natural frequency is outside the operating range. However, in a permanent magnet synchronous motor, the pole passing frequency caused by electromagnetic force is twice the electrical frequency, and from this perspective, the pole passing frequency at 54,792 rpm coincides with the 1st natural frequency of the test motor and jig. There are two methods to avoid resonance: increasing the stiffness of the jig to increase the natural frequency or quickly passing through the resonance point. However, there is a limit to increasing the stiffness of the jig, so the method of accelerating quickly near the resonance point was chosen. Additionally, since the rotor of the test motor is coupled with the rotor of the inline torque sensor and generator, a dynamic analysis of the entire rotor system was conducted for stability analysis. Figure 9 shows the entire rotor system of the M/G dynamometer, and Figure 10 shows the results of the rotordynamics. 1X is the ratio of rpm to frequency of the shaft's rotating speed, and the backward whirl (BW) and forward whirl (FW) modes diverge as the rotational speed rises. If the FW frequency is equal to the 1X line, rotor resonance occurs, and this is known as the critical speed. It was determined that the rotor's 1st critical speed (90,404 rpm) was higher than its operating speed, as shown in Figure 10. The separation margin, which is the difference between the critical speed and operational speed, was around 29.15%, which was adequate to meet American Petroleum Institute (API) standards [33] and recommended practice [34]. The structural stability of the dynamometer was confirmed through two stability analyses, and the dynamometer was constructed based on the 3D model, as shown in Figure 11. The dynamometer experiment results will be discussed in the following section.

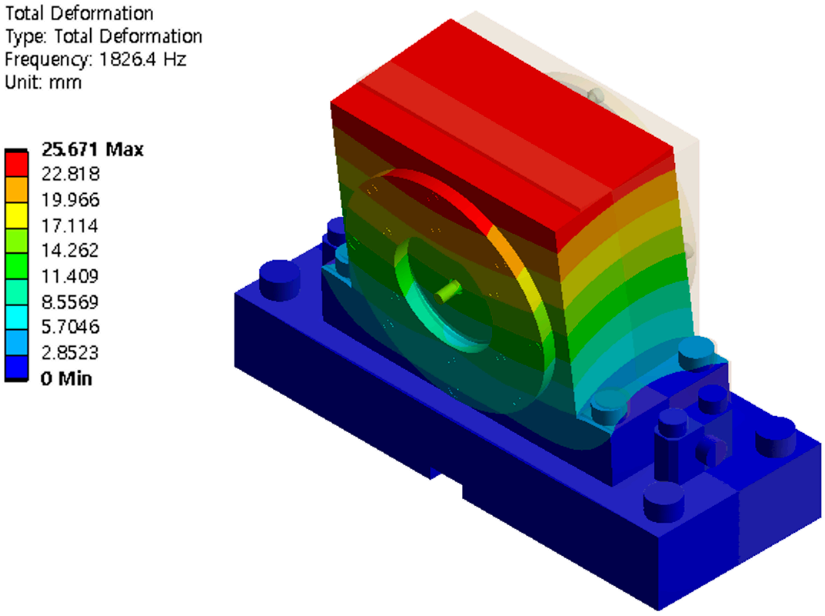

Figure 8. Result of modal analysis for test motor and jig of M/G dynamometer.

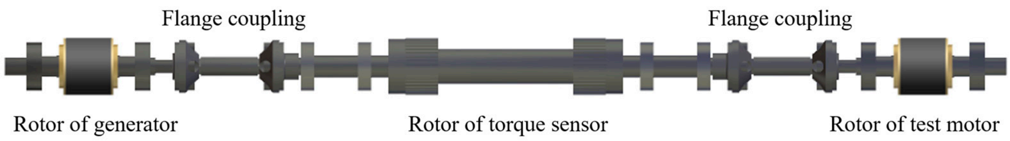

Figure 9. Rotor system of M/G dynamometer with high-speed torque sensor.

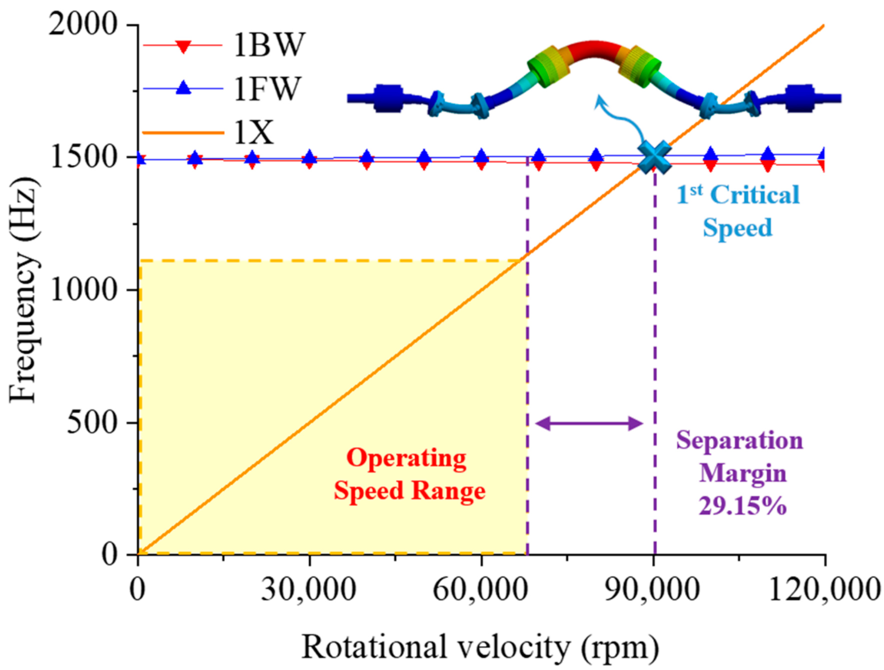

Figure 10. Result of rotordynamics for M/G dynamometer.

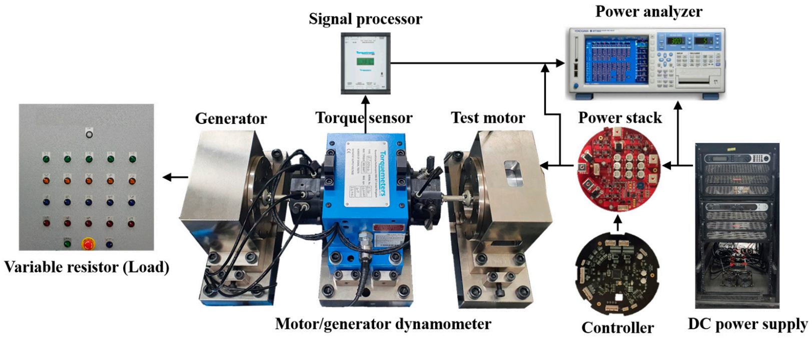

Figure 11. Configuration of motor/generator dynamometer with high-speed torque sensor.

3.2. Eddy Current Brake Dynamometer

As another method of measuring the performance of the motor, instead of using an in-line torque sensor, the test motor was fixed to a cradle base structure, and a dynamometer was constructed using an eddy current brake. A stator and a rotor are the two main parts of the eddy current brake dynamometer. A magnetic field is created by a number of electromagnets inside the stator, which is stationary. Eddy currents that are induced in the rotor as it rotates produce an opposing magnetic field that slows the rotor down. The eddy current brake dynamometer used in this paper was Magtrol's 2WB43. The structural stability was determined by conducting a modal analysis of the test motor and jig as well as the rotordynamics of the rotor of the test motor and the rotor of the eddy current brake dynamometer, using the same method as the stability analysis of the M/G dynamometer previously. Figure 12 shows the modal analysis results for the test motor and jig, where the 1st natural frequency of the motor and jig was 1787 Hz. From the perspective of machine frequency, the 1st natural frequency is higher than the frequency of maximum operating speed. However, the pole-passing frequency at 53,610 rpm coincides with the 1st natural frequency of the test motor and jig. Since the 1st natural frequency is below the frequency of the maximum operating speed, it was confirmed that it must be accelerated and passed through at 53,610 rpm to avoid resonance. Figure 13 presents the entire rotor system of the eddy current brake dynamometer with the rotor of the test motor. Referring to Magtrol's data sheet, the maximum allowable speed for the eddy current brake dynamometer to be used is 65,000 rpm. However, considering the stability, the maximum operating speed was set to 60,000 rpm. The rotational analysis results at that speed are shown in Figure 14. The 1st critical speed at which the bending mode of the rotary shaft system appears was 86,605 rpm, and the separation margin was 44.34%, indicating that it was more than 20%, the separation margin value recommended by the API standard, and also confirming that it was structurally stable. The dynamometer was constructed based on the 3D model shown in Figure 15.

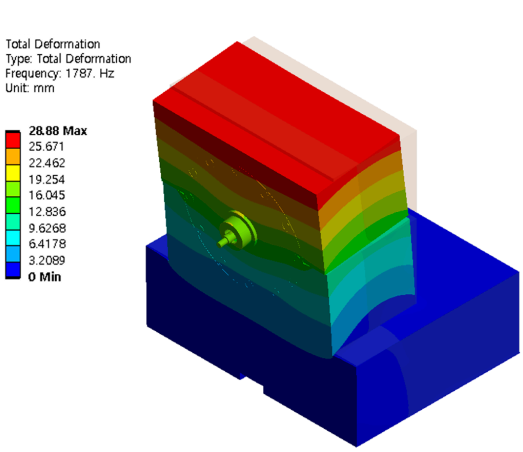

Figure 12. Result of modal analysis for test motor and jig of eddy current brake dynamometer.

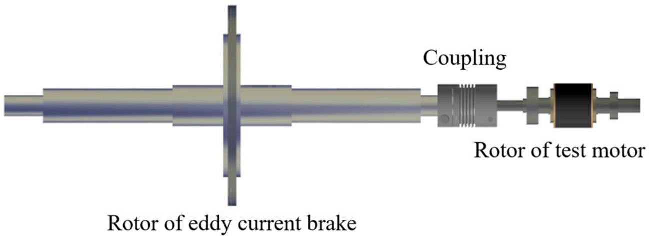

Figure 13. Rotor system of eddy current brake dynamometer with test motor.

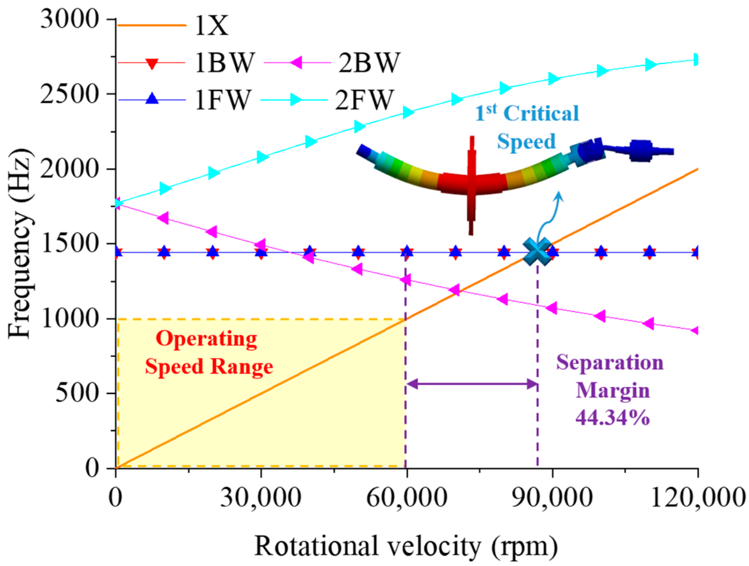

Figure 14. Result of rotordynamics for eddy current brake dynamometer.

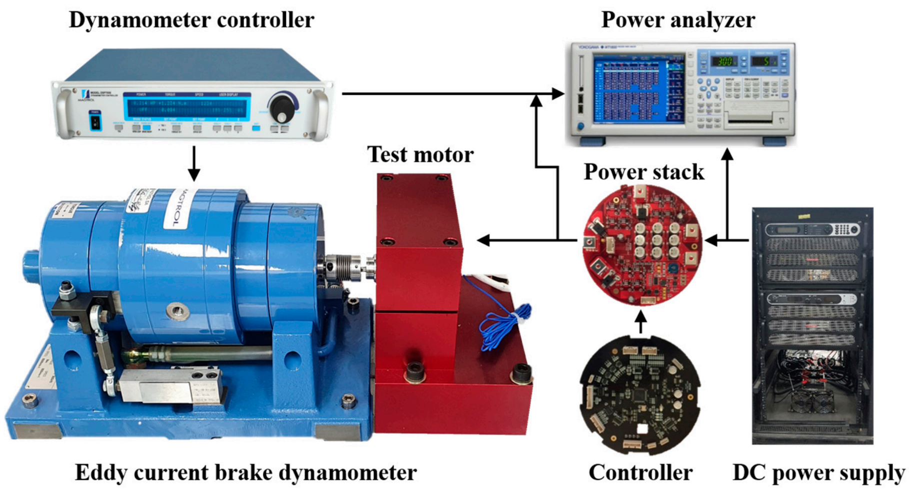

Figure 15. Configuration of eddy current brake dynamometer.

3.3. Inertial Dynamometer

Finally, a dynamometer was constructed that uses the method that measures torque by utilizing the moment of inertia for the motor's rotor and angular acceleration. The inertial dynamometer used in this paper was an inertial dynamometer from MEA Testing System Ltd., an Israeli company. To measure the moment of inertia of the rotor, the flywheel provided was connected to the rotor. The speed of the motor is rapidly accelerated under no load to obtain torque and output power through the moment of inertia and angular acceleration, allowing us to obtain the overall performance of the motor. This is a fairly simple configuration compared to the previous two dynamometer systems, and it is known to be suitable for use in quality control (QC), research and development (R&D) divisions, and the end of the production line due to its simple test procedure and short inspection time. As with the previous two dynamometer stability analysis procedures, the inertial dynamometer was also subjected to the same stability analysis. Figure 16 shows the modal analysis results of the test motor and jig to be used for the inertial dynamometer. The 1st natural frequency was 3587.6 Hz, which was higher than the mechanical excitation frequency (1166.67 Hz) and the pole-passing frequency (2333.33 Hz) at 70,000 rpm, which is the excitation frequency of electromagnetic force, confirming the structural stability within the operating range. As shown in Figure 17, only the motor rotor exists in the inertial dynamometer without an additional rotor. The rotor analysis was performed with the rotor system of the inertial dynamometer, as shown in Figure 18. The results of the analysis showed there was no critical speed in the operating area, the 1st critical speed was 211,290 rpm, and the separation margin was 202.74%. This confirms the structural stability during the test. The inertial dynamometer that was constructed based on the above information is shown in Figure 19.

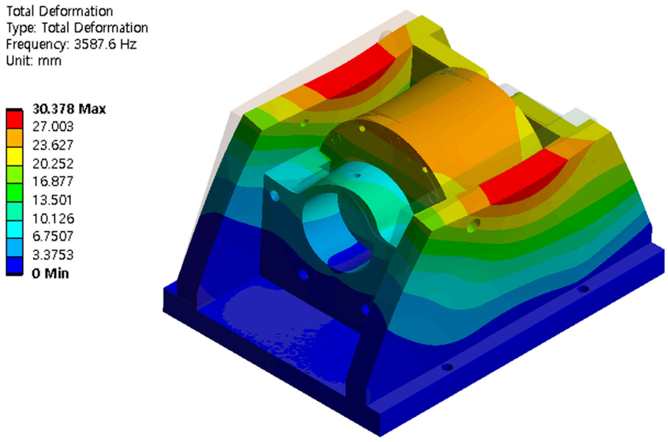

Figure 16. Result of modal analysis for test motor and jig of inertial dynamometer.

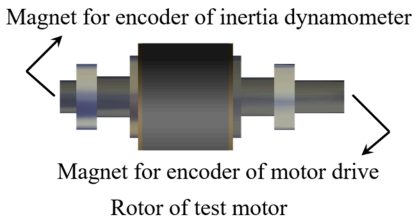

Figure 17. Rotor system of inertial dynamometer.

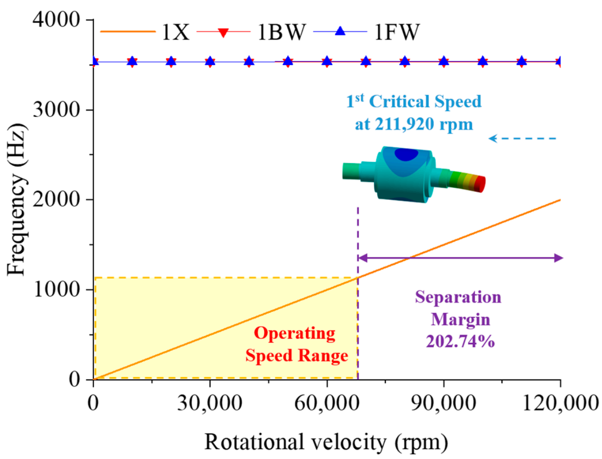

Figure 18. Result of rotordynamics for inertial dynamometer.

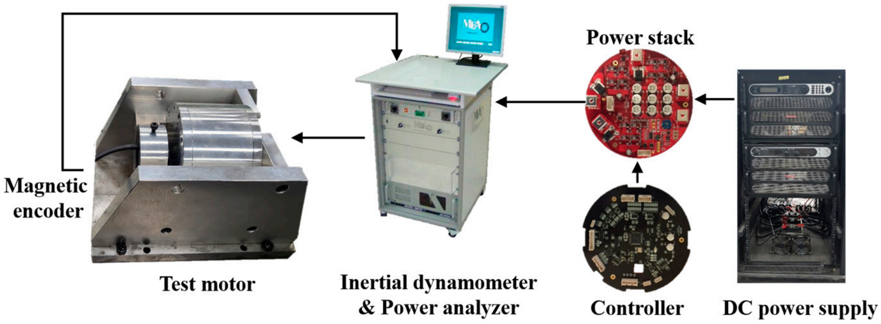

Figure 19. Configuration of inertial dynamometer.

4. Results of Various Experiment Methods

4.1. M/G Dynamometer with High-Speed Torque Sensor

As shown in Figure 11, the M/G dynamometer was configured using a high-speed torque sensor, and a variable resistance load was connected to the generator. The test motor was speed controlled. When the variable resistance value was changed, the current produced by the generator also changed, thereby changing the torque from the generator. In other words, when the variable resistance value is reduced, the current of the generator increases, causing the torque to increase, and when the variable resistance value is increased, the current decreases, causing the torque to decrease. This feature was utilized to adjust the torque load, and the resistance value was maintained to be the same as that of the dynamometer using the reaction torque sensor in Figure 4. The speed was tested from 10,000 rpm, which is the idle speed of the electric turbocharger, to 70,000 rpm, which improves low-speed and transient performance, and the experiment results are shown in Figure 20.

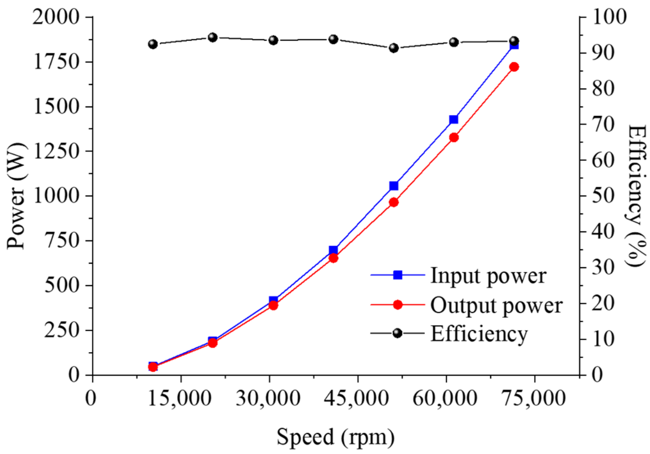

Figure 20. Experiment result of M/G dynamometer with high-speed torque sensor.

4.2. Eddy Current Brake Dynamometer

As shown in Figure 15, the eddy current brake dynamometer was configured, and after tuning the gain of the speed controller, the test motor was driven by speed control in the same manner as before. The torque load was created using the eddy current brake, and the test was conducted from 10,000 rpm, which is the idle speed of the electric turbocharger, to 60,000 rpm, which is below the maximum allowable speed of the eddy current brake dynamometer. The test results are shown in Figure 21.

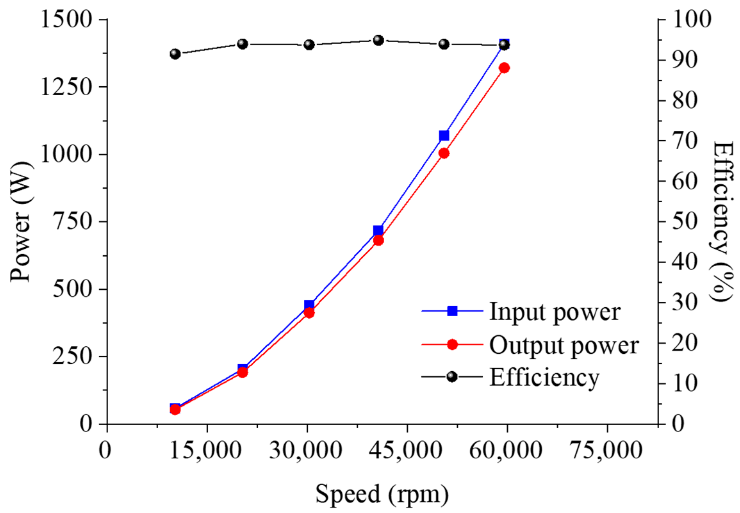

Figure 21. Experiment result of eddy current brake dynamometer.

4.3. Inertial Dynamometer

The moment of inertia for the rotor of the test motor was measured before configuring the inertial dynamometer, and then, the dynamometer was constructed, as shown in Figure 19. Since the moment of inertia of the entire rotor system of each dynamometer is different, the gain of the speed controller must be tuned according to the dynamometers. In particular, in the case of the inertial dynamometer, since the angular acceleration must be obtained by accelerating in a short time period, the test motor was driven under no-load conditions after gain tuning. In the same way as the M/G dynamometer test using the high-speed torque sensor, the test started at 10,000 rpm and proceeded up to 70,000 rpm, and the test results are shown in Figure 22.

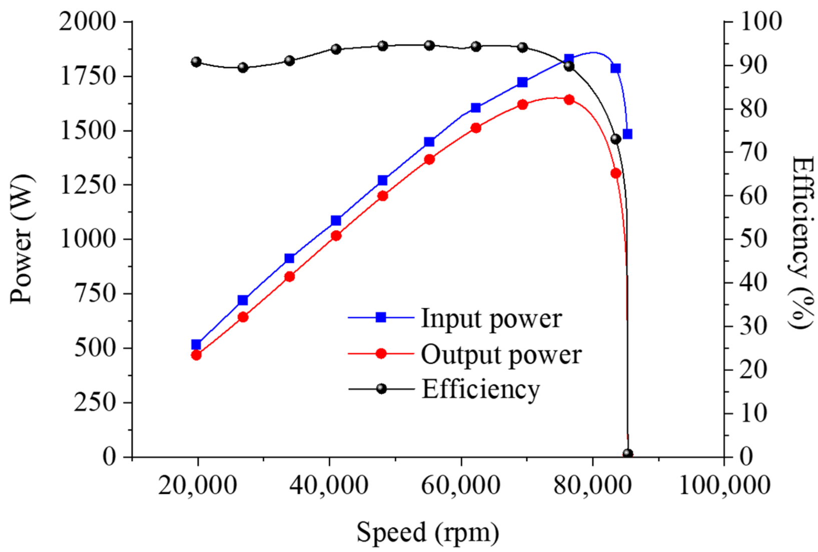

Figure 22. Experiment result of inertial dynamometer.

4.4. Comparison of Test Results of Three Dynamometers

Table 3 shows the test results for the high-speed motors performed on three dynamometers based on the test results using the reaction torque sensor in Section 2. The output power of the M/G dynamometer using the high-speed torque sensor at 70,000 rpm in Table 3 appeared to be almost identical to the reference data when performed with a resistive variable load. However, there was a difference of about 0.9% in efficiency, which seems to be due to the difference in the inertial moment of the entire rotor system of the dynamometer, which requires more input current to achieve the same output power. Compared with the inertial dynamometer and reference data at 70,000 rpm, there was a difference of about 0.074 kW in output power. As the torque was calculated with the rotor's moment of inertia and angular acceleration, the torque and power seemed to differ because of the difference in angular acceleration resulting from the gain tuning of the controller and the rotor's moment of inertia, and the efficiency showed an error of 0.4%. When examining the test results of the reference data and three dynamometers at 60,000 rpm, the output power of the M/G dynamometer and the eddy current brake dynamometer appeared to be similar, but there was a discrepancy of 0.172 kW in the inertial dynamometer. However, this seems to have been caused by the same reason described earlier. In terms of efficiency, the reference data, the results of the eddy current brake dynamometer, and the results of the inertial dynamometer were almost identical, while the M/G dynamometer showed an error of 0.7%, which was attributed to the same cause of the error at 70,000 rpm.

Table 3. Comparison of test results of three dynamometers.

Item		FEA	Reference (Figure 4)	M/G	Eddy Current Brake	Inertial
Output power (kW)	70,000 rpm	1.70	1.70	1.722	-	1.626
	60,000 rpm	1.30	1.30	1.327	1.321	1.472
Efficiency (%)	70,000 rpm	93.74	94.2	93.3	-	93.8
	60,000 rpm	93.68	93.7	93.0	93.7	93.8

Each dynamometer was evaluated for five categories: stability, accuracy, test time, dynamometer configuration cost, and installation difficulty. Based on the stability analysis results, equipment price, and test results, for each dynamometer, a radar chart was prepared, and this is presented in Figure 23. The higher the stability and accuracy, the better, and the lower the test time, cost, and installation difficulty, the better the characteristics. Although it had the longest test time, the eddy current brake dynamometer was the best in terms of stability, accuracy, cost, and installation difficulty. When considering stability, test time, and ease of installation, the inertial dynamometer is the best option.

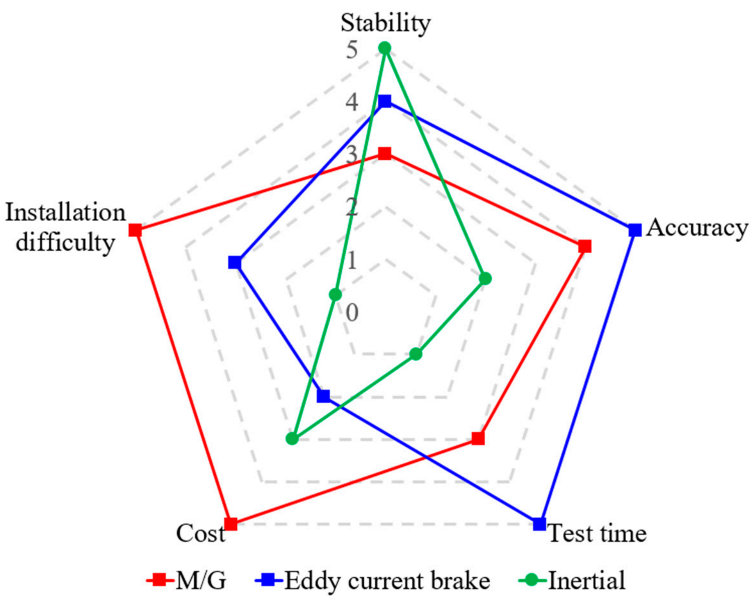

Figure 23. Radar chart of the 5 characteristics of each dynamometer.

5. Conclusions

Since it is not easy to construct a dynamometer to perform load performance testing of a high-speed motor, given the price of the measuring equipment, many studies have compared the analysis results and experimental results under no-load conditions, or they have compared the estimated performance in the high-speed range with the low-speed, light-load results. Unlike the above, this paper proposes three experiment methods to accurately measure the performance of motors in the high-speed range under load conditions up to the rated point, and it compares and analyzes the results. The experiment method of the dynamometer was determined by referring to international standards such as IEC and IEEE. Before constructing the dynamometer, stability analyses were conducted on the dynamometer system itself to prevent safety problems during the experiment. Through modal analysis of the test motor and the jig fixing the test motor, it was determined whether there was a resonance point during the run-up section. For the M/G dynamometer using a high-speed torque sensor and eddy current brake dynamometer, resonance can occur at a specific speed. It was confirmed that resonance avoidance was necessary. In addition, structural stability was also reviewed by evaluating the rotordynamics of the entire rotor system of the three dynamometers. After that, an actual dynamometer was constructed and tested, and the results were comparatively analyzed in Section 4. Since each dynamometer has its strengths and weaknesses, it is important to select an appropriate dynamometer according to the test environment and conditions, and it is expected that the test methods proposed in this paper can be used for load performance tests of various speed motors as well as high-speed motors.

Author Contributions: Conceptualization, T.-W.L. and D.-K.H.; methodology, T.-W.L. and D.-K.H.; software, T.-W.L.; validation, T.-W.L. and D.-K.H.; investigation, T.-W.L.; resources, T.-W.L. and D.-K.H.; data curation, T.-W.L.; writing—original draft preparation, T.-W.L.; writing—review and editing, D.-K.H.; visualization, T.-W.L.; supervision, D.-K.H.; project administration, D.-K.H.; funding acquisition, D.-K.H. All authors have read and agreed to the published version of the manuscript.

Funding: This work was supported by the UST Young Scientist Research Program 2020 through the University of Science and Technology, Republic of Korea (No. 2020YS30) and was supported by the Ministry of Trade, Industry & Energy (MOTIE, Republic of Korea) under the Industrial Technology Innovation Program (No.10062541, "Development of electric compressor to improve low end torque performance and transient performance of 1.6 L grade small diesel engine"). In addition, this research was supported by the Korea Electrotechnology Research Institute (KERI) Primary research program through the National Research Council of Science & Technology (NST) funded by the Ministry of Science and ICT (MSIT, Republic of Korea) (No. 23A01082).

Data Availability Statement: Some or all of the data and the models generated or used during the study are available in a repository or online.

Acknowledgments: This project was conducted jointly with KERI, Keyyang Precision, Hanyang University, and Kookmin University.

Conflicts of Interest: The authors declare no conflict of interest.

Appendix A

Table A1. 1.6-L Vehicle System Parameter.

Description	Specification
Engine type	Diesel
Displacement (L)	1.6
Bore × stroke (mm)	76 × 88
Maximum power (ps/rpm)	115/3400~4500
Maximum torque (kg-m/rpm)	30.3/1500~2500
Compression ratio	15.5
EGR system	High pressure cooled EGR system
After treatment system	LNT + DPF
Induction type	Turbocharged

References

1. Lee, W.; Schubert, E.; Li, Y.; Li, S.; Bobba, D.; Sarlioglu, B. Overview of Electric Turbocharger and Supercharger for Downsized Internal Combustion Engines. *IEEE Trans. Transp. Electrif.* **2017**, *3*, 36–47. [CrossRef]
2. Lee, T.-W.; Hong, D.-K. Electrical and Mechanical Characteristics of a High-Speed Motor for Electric Turbochargers in Relation to Eccentricity. *Energies* **2021**, *14*, 3340. [CrossRef]
3. Arnold, S.; Balis, C.; Barthelet, P.; Poix, E.; Samad, T.; Hampson, G.; Shahed, S.M. *Garrett Electric Boosting Systems (EBS) Program*; Honeywell Turbo Technologies: USA, 2005.
4. Zhao, D.; Stobart, R.; Mason, B. Real-Time Energy Management of the Electric Turbocharger Based on Explicit Model Predictive Control. *IEEE Trans. Ind. Electron.* **2020**, *67*, 3126–3137. [CrossRef]
5. Menegazzi, P.; Wu, Y.; Thomas, V. Design of an electric supercharger for downsized engines. *MTZ Worldw.* **2013**, *74*, 36–41. [CrossRef]
6. Audi Technology Portal. Forced Induction Concept and Electrical System: Electric Powered Compressor (EPC) and 48-Volt Subsystem. 2016. Available online: https://www.audi-technology-portal.de/en/download?file=1416 (accessed on 18 April 2022).
7. Lee, W.; Kim, J.H.; Choi, W.; Sarlioglu, B. Torque Ripple Minimization Control Technique of High-Speed Single-Phase Brushless DC Motor for Electric Turbocharger. *IEEE Trans. Veh. Technol.* **2018**, *67*, 10357–10365. [CrossRef]
8. Breitbach, H.; Metz, D.; Weiske, S.; Spinner, G. *Application and Design of the eBooster from BorgWarner*; BorgWarner Turbo System GmbH: Auburn Hills, MI, USA, 2015.
9. Biwersi, S.; Tavernier, S.; Equoy, S. Electric compressor with high-speed brushless DC motor. *MTZ Worldw.* **2012**, *73*, 50–53. [CrossRef]
10. Noguchi, T.; Kano, M. Development of 150,000 r/min, 1.5 kW Permanent-Magnet Motor for Automotive Supercharger. In Proceedings of the 2007 PEDS, Bangkok, Thailand, 27–30 November 2007; pp. 183–188.
11. Heidrich, T.; Ludwig, F.; Moeckel, A. Investigation of a high-speed drive for turbo-machines. In Proceedings of the Innovative Small Drives and Micro-Motor Systems, 11th GMM/ETG-Symposium, Saarbruecken, Germany, 27–28 September 2017; pp. 1–5.
12. Yamashita, Y.; Ibaraki, S.; Sumida, O.; Ebisu, K.I.; An, I.L.; Ogita, I. Development of electric supercharger to facilitate the downsizing of automobile engines. *Mitsubishi Heavy Ind. Tech. Rev.* **2010**, *47*, 7–12.
13. Ibaraki, S.; Yamashita, Y.; Sumida, K.; Ogita, H.; Jinnai, Y. Development of the 'hybrid turbo', an electrically assisted turbocharger. *Mitsubishi Heavy Ind. Tech. Rev.* **2006**, *43*, 1–5.
14. Shimizu, M. Turbocharger with Electric Motor. U.S. Patent US8882478B2, 11 November 2014.
15. Gödeke, H.; Prevedel, K. Hybrid turbocharger with innovative electric motor. *MTZ Worldw.* **2014**, *75*, 26–31. [CrossRef]
16. Hofbauer, P. Method of Controlling an Electrically Assisted Turbocharger. U.S. Patent US20110022289A1, 27 January 2011.
17. Lim, M.-S.; Kim, J.-M.; Hwang, Y.S.; Hong, J.-P. Design of an Ultra-High-Speed Permanent-Magnet Motor for an Electric Turbocharger Considering Speed Response Characteristics. *IEEE/ASME Trans. Mechatron.* **2017**, *22*, 774–784. [CrossRef]
18. Gill, N. Driving clean technology. In Proceedings of the Cleantech Forum Europe 2012, Munich, Germany, 16–18 April 2012.
19. Tran, H.H.; Richard, B.; Gray, K.; Hall, J.M. Developing a performance specification for an electric supercharger to satisfy a range of downsized gasoline engine applications. In Proceedings of the SAE 2016 World Congress & Exhibition, Detroit, MI, USA, 12–14 April 2016.
20. Lee, T.-W.; Baek, S.-J.; Hong, D.-K.; Lee, K.-H. Simulation and Motor Test Considering Engine Experiment Validation of Electric Turbocharger for 1.6 L Diesel Engine. *IEEE Trans. Transp. Electrif.* **2021**.
21. Hong, D.-K.; Lee, T.-W.; Jeong, Y.-H. Design and Experimental Validation of a High-Speed Electric Turbocharger Motor Considering Variation of the *L/D* Ratio. *IEEE Trans. Magn* **2018**, *54*, 1–4.
22. Hong, D.-K.; Jeong, Y.-H.; Woo, B.-C.; Kim, T.-H. Electric-mechanical performance analysis of high speed motor for electric turbo charger. *Int. J. Appl. Electromagn. Mech.* **2018**, *57*, 125–133. [CrossRef]
23. Hong, D.-K.; Jeong, Y.-H. Multiphysics Analysis of a High Speed PMSM for Electric Turbo Charger. *Int. J. Appl. Electromagn. Mech.* **2019**, *59*, 835–843. [CrossRef]
24. Bumby, J.R.; Spooner, E.; Jagiela, M. Equivalent circuit analysis of solid-rotor induction machines with reference to turbocharger accelerator applications. *IEE Proc.-Electr. Power Appl.* **2006**, *153*, 31–39. [CrossRef]
25. Gerber, M.; Gilson, A.; Depernet, D.; Dubas, F.; Espanet, C.; Andrieux, G. Coupled Electronic and Magnetic Fast Simulation for High-Speed Permanent-Magnet Drive Design. In Proceedings of the IEEE Vehicle Power and Propulsion Conference (VPPC), Hangzhou, China, 17–20 October 2016.
26. Jung, D.-H.; Lee, J.-K.; Kim, J.-Y.; Jang, I.S.; Lee, J.; Lee, H.-J. Design Method of an Ultrahigh Speed PM Motor/Generator for Electric-Turbo Compounding System. *IEEE Trans. Appl. Supercond.* **2018**, *28*, 1–4. [CrossRef]
27. Farhan, A.; Johnson, M.; Hanson, K.; Severson, E.L. Design of an Ultra-High Speed Bearingless Motor for Significant Rated Power, In Proceedings of the 2020 IEEE Energy Conversion Congress and Exposition (ECCE), Detroit, MI, USA, 11–15 October 2020.
28. Ou, J.; Liu, Y.; Doppelbauer, M. Comparison Study of a Surface-Mounted PM Rotor and an Interior PM Rotor Made From Amorphous Metal of High-Speed Motors. *IEEE Trans. Ind. Electron.* **2021**, *68*, 9148–9159. [CrossRef]
29. Ou, J.; Liu, Y.; Breining, P.; Gietzelt, T.; Wunsch, T.; Doppelbauer, M. Experimental Characterization and Feasibility Study on High Mechanical Strength Electrical Steels for High-Speed Motors Application. *IEEE Trans. Ind. Appl.* **2021**, *57*, 284–293. [CrossRef]

30. *IEC 60034-2-1*; Rotating Electrical Machines—Part 2-1: Standard Methods for Determining Losses and Efficiency from Tests (Excluding Machines for Traction Vehicles). International Electrotechnical Commission: Geneva, Switzerland, 2014.
31. *IEEE Std 115*™; IEEE Guide for Test Procedures for Synchronous Machines Including Acceptance and Performance Testing and Parameter Determination for Dynamic Analysis. IEEE: Piscataway, NJ, USA, 2019.
32. van Millingen, R.D.; van Millingen, J.D. Phase shift torquemeters for gas turbine development and monitoring, In Proceedings of the ASME 1991 International Gas Turbine and Aeroengine Congress and Exposition, Orlando, FL, USA, 3–6 June 1991.
33. *ANSI/API Standard 610*; Centrifugal Pumps for Petroleum, Petrochemical and Natural Gas Industries. American Petroleum Institute: Washington, DC, USA, 2004.
34. *API Publication 684*; Tutorial on the API Standard Paragraphs Covering Rotor Dynamics and Balancing: An Introduction to Lateral Critical and Train Torsional Analysis and Rotor Balancing. American Petroleum Institute: Washington, DC, USA, 1996.